ACS APPLIED MATERIALS & INTERFACES

www.acsami.org

Research Article

Aerosol-Jet-Printed Graphene Immunosensor for Label-Free Cytokine Monitoring in Serum

Kshama Parate,[‡] Sonal V. Rangnekar,[‡] Dapeng Jing, Deyny L. Mendivelso-Perez, Shaowei Ding, Ethan B. Secor, Emily A. Smith, Jesse M. Hostetter, Mark C. Hersam,[*] and Jonathan C. Claussen[*]

Cite This: *ACS Appl. Mater. Interfaces* 2020, 12, 8592−8603

Read Online

ACCESS | Metrics & More | Article Recommendations | Supporting Information

ABSTRACT: Graphene-based inks are becoming increasingly attractive for printing low-cost and flexible electrical circuits due to their high electrical conductivity, biocompatibility, and manufacturing scalability. Conventional graphene printing techniques, such as screen and inkjet printing, are limited by stringent ink viscosity requirements properties and large as-printed line width that impedes the performance of printed biosensors. Here, we report an aerosol-jet-printed (AJP) graphene-based immunosensor capable of monitoring two distinct cytokines: interferon gamma (IFN-γ) and interleukin 10 (IL-10). Interdigitated electrodes (IDEs) with 40 μm finger widths were printed from graphene-nitrocellulose ink on a polyimide substrate. The IDEs were annealed in CO_2 to introduce reactive oxygen species on the graphene surface that act as chemical handles to covalently link IFN-γ and IL-10 antibodies to the graphene surfaces. The resultant AJP electrochemical immunosensors are capable of monitoring cytokines in serum with wide sensing range (IFN-γ: 0.1−5 ng/mL; IL-10: 0.1−2 ng/mL), low detection limit (IFN-γ: 25 pg/ml and IL-10: 46 pg/ml) and high selectivity (antibodies exhibited minimal cross-reactivity with each other and IL-6) without the need for sample prelabeling or preconcentration. Moreover, these biosensors are mechanically flexible with minimal change in signal output after 250 bending cycles over a high curvature (Φ = 5 mm). Hence, this technology could be applied to numerous electrochemical applications that require low-cost electroactive circuits that are disposable and/or flexible.

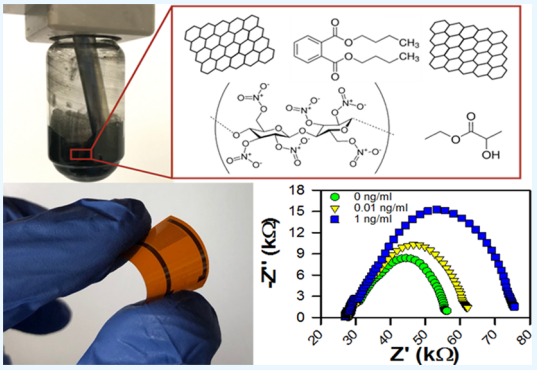

KEYWORDS: *aerosol jet printing, graphene, printed electronics, interdigitated electrode, electrochemical biosensor, cytokines*

1. INTRODUCTION

Printing nanomaterial inks to create low-cost electrical circuits holds significant promise for a wide variety of applications including medical diagnostics, food security, energy storage or energy harvesting devices, and electronic skin or electronic noses due to their ability to be fabricated in a scalable fashion on flexible substrates, including those that are thermally and chemically sensitive (e.g., paper or polymers), without the need for expensive cleanroom processing.[1−9] One of the more promising materials for printed electronics is graphene due to its high surface area, chemical stability, mechanical flexibility, and biocompatibility.[2,10,11] Chemical vapor deposition (CVD) has been a traditional fabrication technique for graphene-based devices.[12] However, this graphene synthesis process and the associated techniques necessary to incorporate the resultant graphene into devices have limited the widescale use of CVD graphene for electronic devices. For example, CVD processing has high energy costs and low yields due to the use of high-temperature and low-pressure furnace synthesis protocols. Moreover, the subsequent graphene film transfer process, needed to relocate the graphene to a more electrically and electrochemically inert substrate, is tedious and can significantly damage the graphene film.[12,13] Finally, additional patterning steps via photolithography are required to fabricate CVD graphene devices over a large area.

A more scalable method of obtaining graphene is through liquid-phase exfoliation of graphite.[14] This method produces graphene dispersions, which can consequently be formulated into graphene inks for a variety of printing applications, such as screen printing and inkjet printing, for large-scale manufacturing.[15,16] Conventional screen printing that uses a squeegee to force ink through patterned perforations on a metal stencil typically results in low-resolution circuits (100 μm line resolution or higher).[2,15,17] More recent advances in screen printing has realized high-resolution circuits (3.2 μm) through the use of lithographically patterned composite silicon molds.[18] However, since the fabrication of these high-resolution stencils requires cleanroom processing (e.g., photolithography and

Received: December 7, 2019
Accepted: January 6, 2020
Published: February 10, 2020

https://dx.doi.org/10.1021/acsami.9b22183
ACS Appl. Mater. Interfaces 2020, 12, 8592−8603

reactive ion etching), they are not compatible with high-throughput, conventional screen printing instruments.

Inkjet printing is a scalable printing process compatible with roll-to-roll processing.[19] Indeed, we have recently demonstrated that inkjet-printed graphene electrodes can be used for electrochemical biosensing such as hydrogen peroxide sensing and ion sensing in sweat.[10,20] However, due to the limited spatial resolution of high-throughput inkjet printing, these biosensors have been limited to macroscale electrode designs that can be functionalized with enzymatic and ion selective membranes for subsequent amperometric or cyclic voltammetric sensing modalities. These macroscale electrode geometries are not well-suited for high-resolution impedance-based measurements often performed with interdigitated electrodes (IDEs) fabricated on the micron scale and functionalized with affinity-based biorecognition agents such as antibodies. Moreover, the favorable IDE properties such as high signal-to-noise ratio, fast response time, and favorable reaction−diffusion kinetics improve as the IDE finger comb geometries are decreased to a scale of tens of microns.[21−23] In order to attain such high line resolution with printed electrodes, researchers have begun using various hybrid printing techniques that require pre- or post-patterning steps, such as inkjet maskless lithography, selective sintering, and transfer printing.[1,18,24] For example, high-resolution, inkjet-printed patterns require an additional sacrificial layer that is used in lift-off patterning of graphene or used as a deposition adhesion promoter.[1,16] While these techniques can produce high-resolution conductive traces (20−60 μm line widths), the additional patterning steps complicate a roll-to-roll manufacturing process. Other high-resolution inkjet printing strategies rely on the fluid dynamics of the coffee-ring effect, which can create 5−10 μm wide conductive traces or sub-10 micron channel lengths between printed features, but possible device geometries are still limited by the droplet radius and drying patterns or an additional lift-off process that makes the technique less scalable than inkjet printing alone.[25−27] Therefore, a need exists to create high-resolution graphene biosensor circuits that are compatible with high-throughput manufacturing.

Aerosol jet printing (AJP) is a direct-write additive manufacturing technique that eliminates the need for masks, stencils, or hybrid techniques to produce patterned circuits with high spatial resolution.[28,29] High-resolution lines with widths less than 50 μm can be achieved by AJP, which consequently enables a wide variety of components in printed electronics.[30] Additionally, AJP is a more versatile printing technology as a wider range of inks can be used without the concerns of piezoelectric inkjet nozzle clogging.[31,32] Due to minimal constraints on ink properties, AJP can be used to print diverse materials, ranging from ceramics to carbon nanomaterials to organic semiconductors.[33−35] AJP also accommodates a broad number of substrates including conductors, semiconductors, dielectrics, and mechanically flexible polymers.[31] It should also be noted that AJP has been used previously to pattern graphene interconnects[28,36] and to create composite AJP carbon and metallic electrodes for biosensing purposes,[37−39] but research on more complex all-graphene devices including implementation into biosensors is still lacking.

Here, we demonstrate the first aerosol-jet-printed flexible graphene IDE for electrochemical biosensing. A graphene-nitrocellulose ink was printed on a flexible polyimide film (Kapton) in an IDE pattern by aerosolizing graphene and depositing the aerosol mist in highly focused lines. The IDEs are composed of 50 microbands that are 40 μm in width, which is lower than previously developed inkjet-printed graphene electrodes or laser-induced graphene electrodes that are not lithographically patterned.[16,40] Prepared electrodes were thermally annealed in a CO_2 environment to create surface carboxyl groups on the graphene IDE that act as subsequent chemical handles for covalently linking bovine antibodies for interferon gamma (IFN-γ) and interleukin-10 (IL-10) cytokine monitoring.

The rapid monitoring of both IFN-γ and IL-10 is important for a wide range of diseases as it is associated with monitoring immune system functions.[41] For example, in humans, a ratio of low IFN-γ/IL-10 has been associated with progression to severe mycobacterial infection, which can lead to tuberculosis, HIV, and rheumatoid arthritis.[42,43] Such IFN-γ/IL-10 monitoring may also be important for early, symptom-free detection of the contagious and fatal disease in cattle called Johne's disease, which infects the small intestine and is caused by *Mycobacterium avium* subspecies *paratuberculosis*.[22,44,45] Moreover, both IFN-γ and IL-10 have been measured individually for diagnosis and prediction of disease outcomes in humans with tuberculosis, systemic meningococcal disease, and hepatitis C.[46−48]

2. RESULTS AND DISCUSSION

2.1. Printed Biosensor Development. The first step to the fabrication of the printed biosensors was to create a graphene ink that was formulated for AJP (Figure 1a). First, a 1:1 graphene:nitrocellulose powder was prepared through exfoliation and flocculation techniques that are reported in our previous works.[49,50] It is important to note here that the pure graphene flakes are exfoliated from graphite through a natural

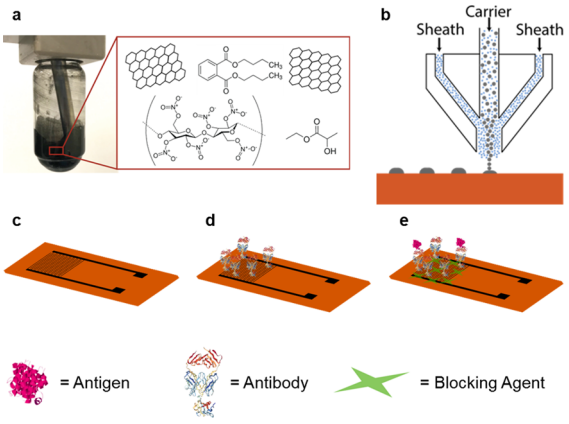

Figure 1. Schematic representation of fabrication and biofunctionalization of the AJP graphene IDE. (a) Schematic demonstrating the graphene ink formulation for aerosol printing. (b) Aerosol jet printing mechanism of the graphene ink illustrating a sheath gas enveloping the carrier flow of aerosolized graphene ink particles for focusing the ink to a desired diameter. (c) AJP graphene IDE on a polyimide (Kapton) sheet. (d) Antibodies selective to IL-10 or IFN-γ are immobilized on the carboxyl group functionalized graphene surface using *N*-(3-dimethylaminopropyl)-*N*′-ethylcarbodiimide/*N*-hydroxysuccinimide (EDC/NHS) chemistry. (e) The remaining exposed surface of the graphene sensor is covered with the blocking agent (mixture of bovine serum albumin (BSA), fish gelatin, and Tween-20) and incubated with antigen.

https://dx.doi.org/10.1021/acsami.9b22183
ACS Appl. Mater. Interfaces 2020, 12, 8592−8603

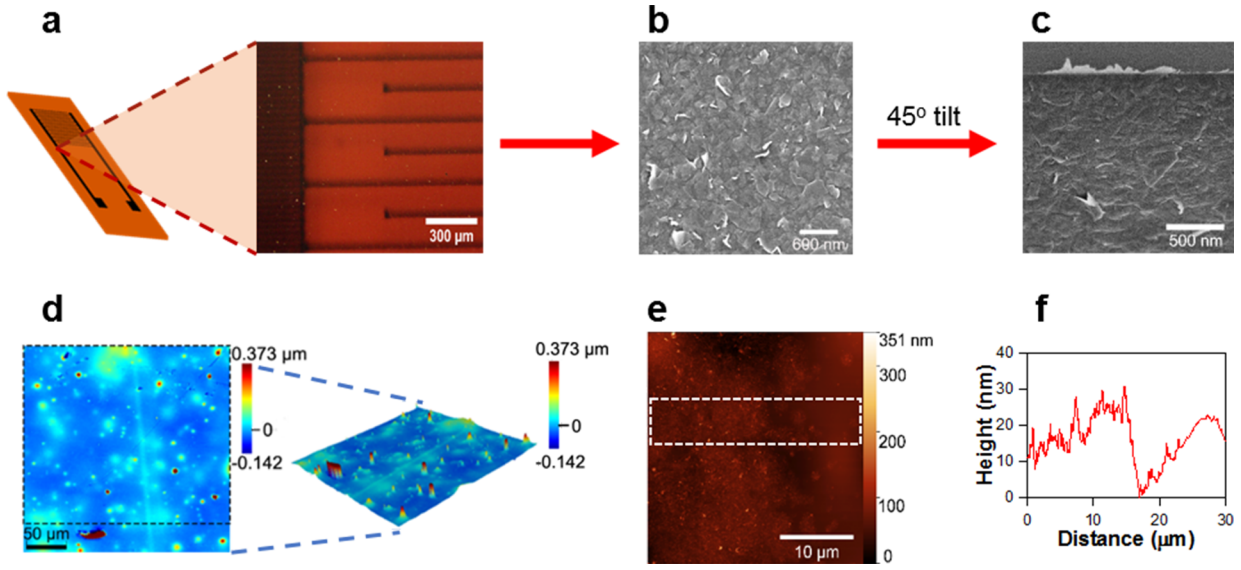

Figure 2. Optical characterization of an AJP graphene IDE. (a) Optical micrograph showing line resolution. SEM micrographs displaying (b) surface morphology of the graphene sheets on the polyimide substrate that is magnified 75000 times. (c) 45°-tilted (magnified 30000 times) top down SEM micrograph of ultrathin (sub-100 nm thick) film printed on SiO_2. (d) The surface irregularity and roughness of bare, as-received Kapton film are observed in 2D and 3D height images. (e) AFM image of the graphene IDE finger and (f) profile of the AFM micrograph showing the average film thickness of the printed graphene as 25 nm averaged across the boxed region in panel (e).

high-shear rotor-stator mixer (Silverson L5M-A) and further ground into a powder with nitrocellulose, which is important to stabilizing graphene in acetone during the exfoliation process. Hence, graphene flakes are used in this printing process in lieu of graphene oxide flakes, which are often obtained through the Hummer method. Other graphene printing techniques typically use graphene oxide flakes and hence typically require additional thermal or chemical graphene oxide reduction processes to make the inks more electrically conductive.[1,10,51,52] In addition, nitrocellulose decomposes into a highly conductive residue after heat treatment, making it a value-added surfactant.[50] The graphene-nitrocellulose powder was found to form a stable dispersion in a 9:1 ethyl lactate:dibutyl phthalate cosolvent system. Dibutyl phthalate has a boiling point of 340 °C, so it prevents aerosol droplets from evaporating completely before deposition on the substrate. Dibutyl phthalate remains in the printed feature until subsequent baking, and its presence allows graphene nanosheets to "relax" into a flat morphology.

A graphene ink with 30 mg/mL solid loading was prepared and filtered through a 3.1 μm membrane prior to printing. A 2 mL aliquot of the graphene ink was pipetted into the ink vial of the printer and ultrasonically atomized. The fluid dynamics of the aerosol jet deposition process are shown in Figure 1b. Aerosolized ink droplets are carried by a nitrogen gas flow toward the deposition nozzle. Before deposition, the carrier gas flow is met by a second nitrogen stream at a higher flow rate, which forms a focusing sheath around the aerosol particles in the carrier stream. The highly focused aerosol droplets, which contain graphene, are then deposited on the substrate below the nozzle. Sheath flow rates of 40−60 sccm, carrier flow rates of 15−45 sccm, and printing speeds of approximately 5 mm/s were tuned to yield thin and continuous traces of graphene ink with minimal satellite droplets on the substrate (Figure S1).

Graphene-based IDEs were printed on a flexible polyimide film (Figure 2a). The devices are designed to maximize the sensing surface area, which increases the sensitivity of the device, while decreasing the channel length (or interfinger spacing) to minimize electrochemical resistance. The electrode design has a finger width of 40 μm, a finger spacing of 100 μm, and 50 fingers, for a total IDE active surface area of 14 mm^2. This 40 μm line resolution is lower than previous direct-write graphene printing processes such as inkjet printing (~60 μm line resolution)[16] or direct-write graphene synthesis processes such as creating laser-induced graphene from polyimide (~75 μm line resolution).[40] The ability to create smaller IDE finger widths has generally been shown to improve the signal-to-noise ratio of the electrodes during electrochemical impedance spectroscopy—the sensing modality used herein to perform the electrochemical cytokine biosensing.[1] The active surface area is defined as the total surface area of printed fingers (finger width × finger length × number of fingers), as these features pose the smallest spacing between electrodes and are dominantly active in subsequent electrochemical measurements. The IDEs were then heat-treated in a tube furnace at 350 °C for 30 min to remove the trapped solvent and drive decomposition of the nitrocellulose into a conductive sp^2 carbon residue.[50]

2.2. Microscopy and Spectroscopy Characterization.

2.2.1. Microscopy Characterization. The film morphology and chemical composition of the heat-treated graphene IDEs were subsequently characterized with confocal laser microscopy, scanning electron microscopy (SEM), atomic force microscopy (AFM), X-ray photoelectron spectroscopy (XPS), and Raman spectroscopy. While the thermal decomposition of nitrocellulose can lead to a porous film under some conditions (Figure S2), SEM images (Figure 2b,c) reveal that the graphene nanosheets are well-aligned in a dense and continuous film in the optimized devices. Coupled with the low film porosity, this degree of flake stacking suggests that the carboxyl functionalization of graphene is mostly limited to the top surfaces of the film, allowing for sp^2-rich content in the bulk of the film and thus high electrical conductivity (1×10^4−7×10^4 S/m). This conductivity measurement is similar to the

https://dx.doi.org/10.1021/acsami.9b22183
ACS Appl. Mater. Interfaces 2020, 12, 8592−8603

conductivity that we obtained previously with blade-coated graphene-nitrocellulose ink (4×10^4 S/m),[50] inkjet-printed graphene-ethyl cellulose ink (2.5×10^4 S/m),[16] and screen-printed graphene-ethyl cellulose ink (1.9×10^4 S/m).[2] It should be noted that Majee et al. acquired a higher conductivity (4×10^4 S/m) with inkjet-printed graphene that also contained ethyl cellulose, but in this case, a higher concentration of graphene (50 mg/mL initial solid loading) was used in the ink formulation.[53]

Next, a bare section of as-received Kapton was scanned at the highest resolution objective of an Olympus confocal laser microscope (50× magnification with 200 nm lateral resolution and 6 nm vertical resolution). The optical image (Figure S3a) shows spots and scratches, but the 3D scan of the film height (Figure 2d) shows additional topography. A roughness measurement of the dashed box region in Figure 2d (see inset) yields a root mean square roughness of 37 nm. The printed graphene line can barely be distinguished from the Kapton film using confocal laser microscopy (Figure S3e), and therefore, AFM was used to measure printed graphene film thickness after heat treatment (Figure 2e,f). Note that the underlying polyimide substrate is wavy and rough, with a root mean square roughness of approximately 40 nm, resulting in AFM scans that appear to have depressed regions in the middle of a printed line (Figure S3). To reasonably measure film thickness, an AFM scanned region with a relatively flat Kapton surface was analyzed. The film thickness was averaged over the boxed region in Figure 2e and found to be 25 nm. This film thickness is several orders of magnitude thinner than those of screen-printed or inkjet-printed devices that can have a thickness of approximately several microns or hundreds of nanometers, respectively. Hence, such thin AJP films translate into lower material consumption (Table S1) for manufacturing the devices.[2,16]

2.2.2. Spectral Characterization. XPS and Raman spectroscopy were next performed to characterize the material properties of the AJP graphene before and after the CO_2 annealing process. Before CO_2 annealing, the graphene IDE consisted of sp^2- and sp^3-hybridized carbon as denoted by the peak at 284.5 eV and carboxyl groups (−COOH) denoted by the peak at 288.5 eV, which contributes only 5% of all the functional groups available on the graphene IDE (Figure 3a). After the CO_2 annealing, the development of complex surface chemistry appears (Figure 3b), including carbide bonds (283.7 eV) and C−C single bonds (285.1 eV) in addition to oxygenated species (i.e., a carboxyl (COOH) group peak at 289.2 eV and a carbonyl group ($R_2C=O$) peak at 287.2 eV) that demonstrate the chemical functionalization of the graphene. The carboxyl and carbonyl groups contribute to 15% of all the functional groups on the surface of the IDE, leading to an increase of 10% of the oxygen-rich groups. These carboxyl and carbonyl groups are essential for further chemical reactions with EDC/NHS that enable covalent binding of the desired antibody with the graphene IDEs.

Next, Raman spectroscopy measurements were performed on the samples before and after annealing with CO_2 in order to characterize the graphitic nature of the samples (Figure 3c). The Raman spectra of the samples exhibited the characteristic bands of graphitic materials including the D band (~1353 cm^{-1}) that is indicative of defects, the G band (~1584 cm^{-1}), and the 2D band (~2702 cm^{-1}) that originates from second-order zone-boundary phonons.[54−56] The intensity ratio I_D/I_G is used as a measure of the defect level in graphite-based

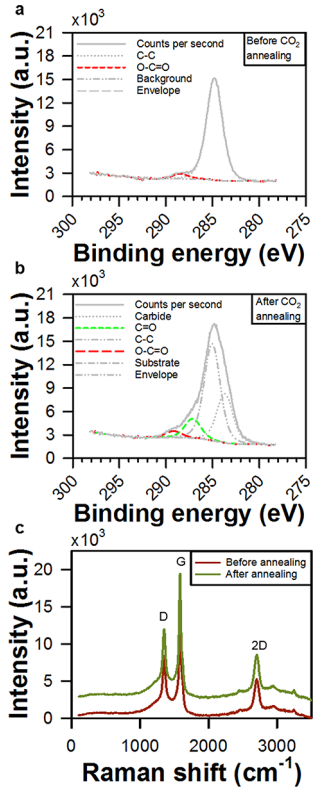

Figure 3. Spectroscopy of the graphene IDE. (a) XPS of graphene IDE before CO_2 thermal annealing. (b) XPS of graphene IDE after CO_2 thermal annealing. (c) Raman spectroscopy of printed graphene IDE before and after CO_2 thermal annealing with D, G, and 2D peaks displayed.

materials,[14,57] and the corresponding values were determined to be 0.49 ± 0.02 and 0.48 ± 0.01 for the sample before and after CO_2 annealing, respectively, which suggest that the CO_2 annealing does not induce significant physical defects or cause material removal (Figure S5) in the samples. The calculated I_{2D}/I_G ratios for unprocessed and processed samples are 0.34 ± 0.02 and 0.36 ± 0.01, respectively, suggesting that the graphitic character of the electrodes is not significantly affected by the CO_2 annealing process.[58]

2.3. Electrical and Electrochemical Characterization. The electrical and electrochemical performances of the graphene IDEs were next characterized to assess the potential of the printed graphene IDEs for biosensing. First, it was demonstrated that AJP can be used to print features with sub-micron thickness. As printed graphene films are known to be percolating networks,[28,59] the relationship between printed film morphology and film conductivity was investigated for aerosol-jet-printed graphene lines with sub-micron thickness. The printing speed and number of printing passes are two straightforward ways to control the thickness and width of printed lines. First, lines were patterned on a Kapton substrate at various printing speeds. Both line thickness and line width are a function of printing time (units of s/mm), which is the inverse of printing speed (mm/s) (Figure 4a). Line thickness, in particular, varies linearly with printing time. Lines of various thicknesses were also achieved using 1 to 30 printing passes.

The conductivities of these lines were investigated as a function of film thickness (Figure 4b). Graphene line conductivity increases with film thickness until approximately 200 nm thickness, after which the conductivity declines. This

https://dx.doi.org/10.1021/acsami.9b22183
ACS Appl. Mater. Interfaces 2020, 12, 8592−8603

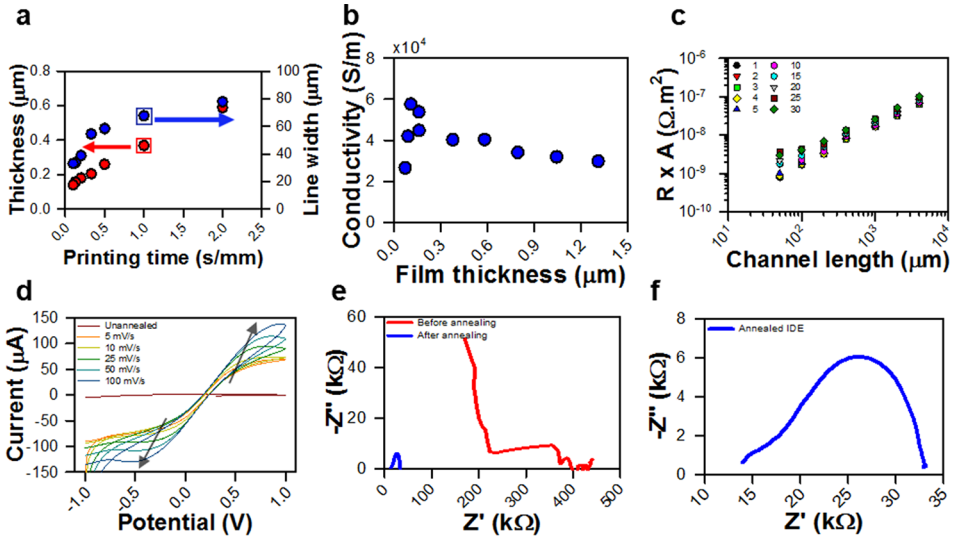

Figure 4. (a) Analysis of several lines printed at 55 sccm sheath flow, 35 sccm carrier flow, and various print speeds shows that the line thickness and line width both vary with printing time (s/mm), which is the inverse of printing speed (mm/s). (b) A plot of conductivity vs maximum film thickness for graphene lines printed on Kapton shows that conductivity increases with film thickness up to about 200 nm before declining. (c) Relationship of resistance multiplied by cross-sectional area vs dimensions of the printed graphene line analogous to an IDE finger for various printing passes (indicated by the legend, i.e., 1, 2, 3, 4, 5, 10, 15, 20, 25, 30). The slope of the plot denotes resistivity of printed graphene. Electrochemical characterization of the graphene IDE showing (d) cyclic voltammetry (CV) before CO_2 annealing and after CO_2 annealing at scan rates of 5, 10, 25, 50, and 100 mV/s and (e) Nyquist plot acquired from electrochemical impedance spectroscopy (EIS) before and after CO_2 thermal annealing. (f) Magnified version of the Nyquist plot of the annealed IDE as shown in the lower-left corner in panel (e) displays a characteristic semicircular Nyquist plot.

behavior can be explained by investigating the film morphology of graphene lines with different thicknesses. As shown by SEM analysis, thin (<100 nm thick) printed lines show a percolating, non-porous microstructure (Figure S2a,b), while thicker films (~1 μm thick) are more porous (Figure S2c,d). This porosity likely emerges during the heat treatment step, as the pyrolysis of nitrocellulose evolves gases that create an open microstructure. The porosity is not accounted for when calculating the cross-sectional area of the printed line, which causes the calculated conductivity to be less than the true value. Furthermore, the porous regions in thicker films may have poorer intersheet contacts, which contribute to lower conductivity despite the amorphous carbon residues. Thus, the use of nitrocellulose in the ink formulation may explain why the conductivity of printed graphene lines does not match the percolation theory as shown by another study (Jabari and Toyserkani).[28] This trend is observed for graphene lines printed on SiO_2 as well as Kapton, indicating that substrate roughness does not influence the film conductivity (Figure S4). This result informed our decision to print IDEs with a single pass, as to form thin films with negligible porosity.

After printing and baking, the graphene IDEs were subjected to a preliminary electrical quality test. A multimeter was used to check the IDEs for low resistance (<10 kΩ) over one side of the ~2 cm long electrode and for shorting pathways between the two electrodes of a single device. Devices passing this screening test were used in subsequent electrochemical experiments. Additionally, transmission line measurements were used to calculate the resistivity of graphene fingers/lines that were printed at the same conditions as the IDEs. The electrical resistance of the graphene lines scales linearly with channel length up to 4 mm, and the resistivity is calculated to be in the range of 1.4×10^{-5}–10^{-4} Ω m (Figure 4c) or an electrical conductivity in the range of 1×10^4–7×10^4 S/m. These results compare favorably with other graphene printed devices.[28,50] The millimeter-scale high conductivity indicates that the graphene nanosheets and amorphous carbon residue form a well-connected matrix over electronically large distances. Further improvements in conductivity are possible when the graphene electrode thickness is increased above 100 nm,[28] but limiting the thickness to 25 nm consumes less material and minimizes printing time without compromising biosensor performance (Tables S1–S3).

The CO_2 annealing process was used to improve the electroactive nature of the printed graphene IDEs from a negligible response to one that is electrochemically active. As mentioned previously, XPS results (Figure 3) showed that the graphene surface is becoming richer in oxygenated species (carboxyl and carbonyl groups) following CO_2 annealing, although the overall defect density remains low. The π-electron cloud on the carboxyl and carbonyl groups helps in the heterogeneous electron transfer between the electrode and the redox probe, and thus, the electrocatalytic nature of the electrodes was improved by performing this CO_2 annealing process.[60] The electrochemical characterization of the graphene IDE was performed by both cyclic voltammetry (CV) and electrochemical impedance spectroscopy (EIS) to determine its heterogeneous electron transfer capability. The CV was performed at scan rates of 5, 10, 25, 50, and 100 mV/s in a 5 mM ferro/ferricyanide probe. As noted in Figure 4d, the graphene IDE before CO_2 annealing does not show an electrochemical response at a scan rate of 100 mV/s since the CV displays near-zero heterogeneous electron transfer due in part to a highly probably lack of sufficient edge plane defects.[61] However, after CO_2 annealing, current peaks appear on the CV due to the increase in the oxygenated species, although Raman shows minimal changes in the surface defects. The occurrence of these peak currents (i_p) with a large separation between them (ranging from ΔE_p = 0.57 to 1.24 V) demonstrates heterogeneous electron transfer kinetics, which is typical of a

https://dx.doi.org/10.1021/acsami.9b22183
ACS Appl. Mater. Interfaces 2020, 12, 8592–8603

multilayer graphene surface functionalized with oxygen groups that has low density of either edge or basal plane defects; this was also demonstrated by Ambrosi and Pumera and Pope et al., who observed a peak-to-peak voltage separation ranging between approximately 0.5 and 1.1 V.[62,63] The effective electrochemical surface area was calculated using the Randles–Ševćik equation (Figure S6) to be 8.4 mm^2. This surface area contributes to a total active site of 60% with respect to the geometric area of the AJP graphene IDE, which is larger than our previously reported work for vertically aligned CNT electrodes.[21] Hence, the CO_2 annealing process significantly improves the electroactive nature of the AJP IDE, which is important to subsequent electrochemical EIS measurements.

EIS characterization was next performed between a frequency range of 0.1 Hz and 100 kHz at a voltage amplitude of 10 mV in a 5 mM ferro/ferricyanide probe. In a Nyquist plot, the high-frequency semicircular region represents the resistance of electron transfer kinetics (R_{ct}) between the redox probe and the electrode surface, corresponding to the diameter of the semicircle. From the Nyquist plot in Figure 4e, the data acquired before CO_2 annealing appears as scattered points, which do not convey any information about the electrochemical properties of the IDE surface. However, after CO_2 annealing, the data form a quantifiable semicircular Nyquist plot (Figure 4f). This can be attributed to the introduction of a higher amount of oxygen functional groups on the IDE, as opposed to the previously low functional group density on the surface, which allows for an ease of exchange of electrons between graphene and the redox probe. Moreover, this system lacks a mass transfer region and features a large charge transfer resistance, $R_{ct} \sim 20$ kΩ (Figure 4f). These electron transfer kinetics are characteristic of a thin film of highly oriented pyrolytic graphite (HOPG) stacking of graphene, which suggests that the CO_2-annealed film consists of mostly basal planes of graphene underneath the functionalized top surface.[64]

2.4. Immunosensing of IFN-γ and IL-10. The IDE was functionalized with an anti-bovine (IFN-γ or IL-10) antibody (Figure 1c,d) for sensing the respective antigens (IFN-γ or IL-10). To avoid nonspecific binding of the antigen with the area of the electrode unoccupied by the antibody, various blocking agents were tested for false positive signals of the biosensor. First, the efficacy of bovine serum albumin (BSA) as a blocking agent was evaluated at various concentrations (0, 0.5, 1, 2%) (Figure S7). However, BSA alone does not prevent nonspecific binding of the antigen. Ultimately, the blocking agent utilized in sensitivity studies of the biosensor was a mixture of 1% BSA, 0.1% Tween-20, and 0.1% fish gelatin, which forms a large-chain protein complex that more extensively covers the bare electrode surface.[65]

The immunosensing performance of the graphene IDE platform was evaluated in a real biological matrix (bovine implant serum, see the Experimental Section) to determine its feasibility for early disease detection in the presence of other proteins. First, the biofunctionalized graphene IDE was incubated with increasing concentration of the respective antigen (IFN-γ or IL-10) prepared in a bovine serum implant. Next, EIS measurements were recorded for each concentration of the antigen added. With every increase in the antigen concentration, the diameter of the Nyquist plot increases, which corresponds to the charge transfer resistance (R_{ct}) between the redox probe and electrode. As the antigen concentration increases, more antigen and antibody bind to form an insulating barrier for the electron transfer across the redox probe and electrode, leading to an increased R_{ct}.[66] Normalized charge transfer resistance is plotted against the concentration of antigen in Figure 5a,b. A linear sensing range

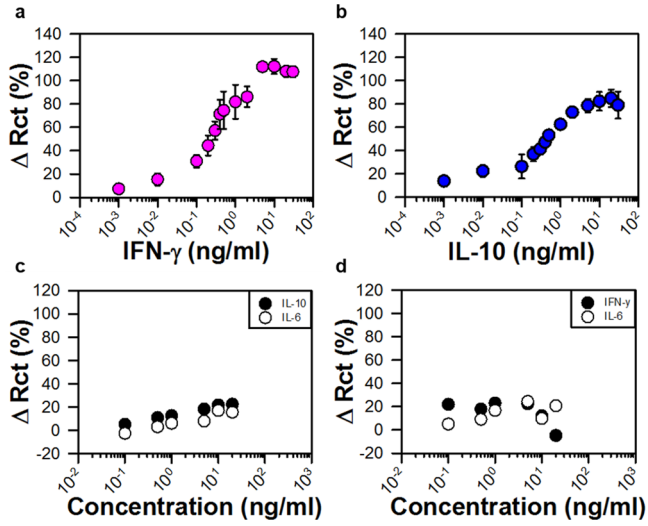

Figure 5. (top) IFN-γ and IL-10 detection using graphene IDE sensors. Percentage change of charge transfer resistance (R_{ct}) with respect to the change in concentrations of (a) IFN-γ and (b) IL-10. Error bars represent standard deviation of the mean calculated from three independently biofunctionalized electrodes with respective bovine monoclonal antibodies. (bottom) Selectivity tests of (c) IFN-γ antibody with IL-10 and IL-6 antigens and (d) IL-10 antibody with IFN-γ and IL-6 antigens.

was obtained by selecting the region of increasing R_{ct} that can be linearly fit with the largest R^2 value. The detection limit was calculated using the regression line equation and considering three times the standard deviation of the background signal (i.e., 3σ). It was found that the linear sensing ranges for IFN-γ and IL-10 were 0.1–5 and 0.1–2 ng/mL, respectively, with detection limits of 25 and 46 pg/mL, respectively (sensitivities of the IDE for IFN-γ and IL-10 were 44.9 and 36.4% per decade, respectively). These sensing ranges cover the lower concentration ranges of IFN-γ detectable in the clinical disease stage and fit in the newly infected to clinical disease stage (in case of IL-10 concentration ranges) of Johne's disease.[44] In addition, these sensing ranges are biomedically relevant; for example, in the case of pulmonary tuberculosis in humans, the mean concentration of IL-10 is 56 pg/mL and that of IFN-γ is 877 pg/mL, whereas in the case of paratuberculosis in cattles, the mean concentration of IFN-γ is 5 ng/mL and that of IL-10 is 8 ng/mL.[44,46,67] As this developed sensor is more sensitive than the latter example, an acquired bovine sample can be easily diluted to acquire the data, and the results can be extrapolated to determine the actual concentration of the cytokines.

Each graphene IDE immunosensor platform was also tested for cross-reactivity with similar antigens (i.e., IFN-γ, IL-10, interleukin-6 (IL-6)). IFN-γ and IL-10 are similar in structure,[68] whereas IL-10 and IL-6 are similar in functionality[69]—making them susceptible for cross-reacting with IL-10 or IFN-γ antibodies. Therefore, the immunosensor functionalized with the IFN-γ antibody was examined for interference with increasing concentration of IL-10 and IL-6, and similarly, the immunosensor functionalized with the IL-10 antibody was

https://dx.doi.org/10.1021/acsami.9b22183
ACS Appl. Mater. Interfaces 2020, 12, 8592–8603

examined for interference with increasing concentration of IFN-γ and IL-6 as shown in Figure 5c,d. In both cases, the percent change in R_{ct} is within 20%, which can be considered as the background signal since the change in R_{ct} is much larger for the same concentration of target antigen. Importantly, the signal shows no clear dependence on the concentration of the interfering antigen, while a much higher change in the signal (~100%) is observed when the appropriate antigen is used. Overall, these results show that the AJP graphene biosensor possesses high selectivity for the immobilized antibody.

2.5. Mechanical Flexibility Measurements. The mechanical flexibility of the IDE was examined by measuring electrical and electrochemical impedance characteristics of a functionalized IDE as a function of bending cycles so that it could be implemented in a wearable or implantable format, such as a small subcutaneous bovine implant.[70] First, the fabricated graphene IDE was mounted on a strip of polyethylene terephthalate (PET) and bent around rods of various diameters (3.18, 7.19, 11.08 mm). The substrate thickness was measured to be 0.25 mm, producing strains (= thickness of substrate/bending diameter) of 0.079, 0.035, and 0.022, respectively. The electrical resistance of the IDE was measured before and after bending (10, 20, 50, 100, 200, 500, 1000 cycles). The fractional change in electrical resistance as a function of bending cycles plotted (Figure 6b) reveals that the change in electrical resistance is almost negligible (<1%), and therefore the electrical characteristics of the device are independent of mechanical flexing cycles.

Next, an IL-10 antibody biofunctionalized graphene IDE was incubated with 10 ng/mL IL-10 antigen and mounted on a PET strip using double-sided adhesive tape. The total thickness of the graphene IDE on the PET assembly was 0.31 mm. The biosensor was flexed around a rod suspended within a 3D-printed trough (Formlabs form 2, 3D printer) so that the biosensor could remain in contact with a layer of buffer solution (phosphate-buffered saline (PBS)) throughout the duration of the experiments to eliminate antibody denaturing due to a dry sensor (Figure 6a). A rod (dia. = 5 mm) resulting in a sensor bending strain of 0.062 was utilized, while the electrochemical signal was recorded following every 50 bending cycles (250 bending cycles were performed). The percentage change in sensor R_{ct} values (derived from the Nyquist plot as shown in Figure S8) of the functionalized biosensor is approximately only 6% for the bending experiments performed with the 5 mm rod, showing robustness of the biosensor when bent severely (Figure 6c). This indicates that this biosensor platform is suitable for use on curvilinear work surfaces.

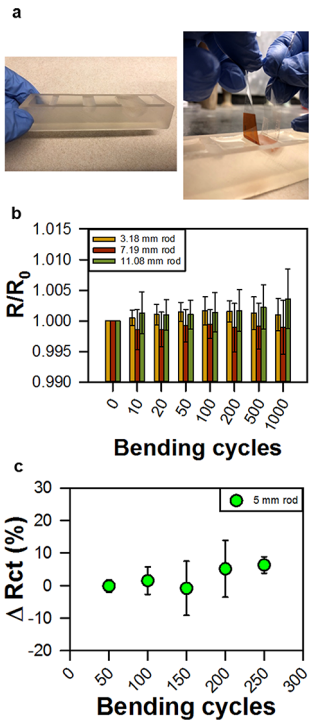

Figure 6. Bending test experiments with the AJP graphene IDE. (a) Photograph of the test setup shows the IL-10 functionalized biosensor bending around a rod that is suspended within a 3D printed trough filled with PBS. (b) Change in the resistance of AJP graphene IDE vs the number of bending cycles without any biofunctionalization. (c) R_{ct} vs the number of bending cycles of the biosensor around a rod (dia. 5 mm).

3. CONCLUSIONS

In conclusion, this work demonstrated the first use of aerosol-jet-printed graphene for biosensing by developing printed interdigitated electrodes with a graphene-nitrocellulose ink. Printed graphene lines demonstrated high electrical conductivity (~10^4 S/m) at low thickness (~25 nm) and across millimeter-scale portions of the film. The top surface of the graphene electrode was functionalized with oxygen-containing groups by annealing in a CO_2 environment while preserving the highly oriented graphitic structure underneath. Graphene biosensors were functionalized with IFN-γ and IL-10 bovine antibodies through EDC/NHS chemistry and were tested in a real biological matrix (bovine minced implant supernatant). These biosensors were able to monitor both IFN-γ and IL-10 in bovine implant serum across wide linear sensing ranges (0.1−5, 0.1−2 ng/mL) with low detection limits (25, 46 pg/mL) and rapid response time (33 min) without the need for preconcentration or labeling steps. Moreover, the biosensor was highly selective toward IFN-γ or IL-10 with negligible cross-reactivity with each other and similar cytokines (i.e., IL-6). Hence, this developed biosensor is well suited for rapid, in-field testing. The developed AJP graphene immunosensors also achieved the best limit of detection and selectivity for an immunosensor that does not require prelabeling or preconcentration and that can monitor both bovine IL-10 and IFN-γ. Moreover, the developed AJP graphene immunosensor overcomes the complexity of laboratory-based multicytokine testing methods, such as fluorescently labelled beads/surfaces functionalized with antibodies commonly associated with Luminex xMAP,[71] fluorescence-enhancing microarrays on plasmonic gold films,[72] and flow cytometric multiplex and enzyme-linked immunosorbent assays[73]; it also circumvents lithographic patterning and electroplating associated with more conventional in-field electrochemical immunosensors created with gold electrodes patterned on printed circuit boards.[74] Important to this work, the developed biosensors detect the biomarkers in the sensing range (0.1−10 ng/mL) that is appropriate for bovine disease paratuberculosis. Such rapid monitoring of these cytokines is clinically important to improve the accuracy of a potential screening test for early-stage detection of diseases, such as Johne's disease in cattles or tuberculosis in humans. By minimizing transportation time, sample storage and handling challenges, and sample degradation, this point-of-care diagnostic sensor will help establish

https://dx.doi.org/10.1021/acsami.9b22183
ACS Appl. Mater. Interfaces 2020, 12, 8592−8603

faster and more accurate treatment solutions for the patient while minimizing errors.

In a broader sense, the AJP graphene electrode created herein could be utilized in a wide variety of applications. The readily functionalized graphene surface and the universality of the antibody functionalization protocol enable sensing of desired analytes without the need of any sample pretreatment. In this context, the developed immunosensor platform could be applied to different sensing paradigms beyond measuring cytokines − such as proteins, bacteria, and viruses for early detection of fatal human diseases like systemic meningococcal disease,[48] cancer,[75] and HIV[76] - or also for detection of food pathogens such as *Escherichia coli*.[77] Additionally, aerosol printing of thin-film graphene IDEs is amenable to high-throughput manufacturing as both graphene exfoliation and printing are scalable processes and are also more suited to graphene recycling as opposed to a high-temperature graphene growth process through chemical vapor deposition, which generally requires cleanroom technology and results in low yields of graphene that are challenging to transfer to substrates that are suitable for device applications.[14,78] Finally, the electrochemical sensitivity and flexibility of the graphene circuits make them potentially well suited for a wide variety of applications including the creation of electrochemical supercapacitors, biofuel/microbial fuel cells, and wearable biosensors.[79−88] In fact, such flexible graphene circuits have been shown to be useful for a wide array of sensor applications including bacteria sensing on tooth enamel, heavy-metal detection via skin-integrated sensors, ion and protein monitoring in sweat, and in solar cells, organic light-emitting diodes, and strain sensors.[88−94]

4. EXPERIMENTAL SECTION

All chemicals and reagents were of analytical grade and handled according to their material safety data sheets. Graphite powder at grade 3061 was purchased from Asbury Graphite Mills (Asbury, NJ, USA). Nitrocellulose (NC), damped with isopropanol, was purchased from Scientific Polymer (Ontario, NY, USA). All solvents were purchased from Millipore Sigma (St. Louis, MO, USA). *N*-(3-Dimethylaminopropyl)-*N*′-ethylcarbodiimide (EDC), *N*-hydroxysuccinimide (NHS), ethanolamine, Tween-20, gelatin from cold water fish skin, and potassium hexacyanoferrate(II) trihydrate were purchased from Sigma-Aldrich (St. Louis, MO, USA). Potassium ferricyanide was purchased from Fisher Scientific (Fair Lawn, NJ, USA). 2-(*N*-Morpholino)ethanesulfonic acid (MES buffer) was purchased from Alfa Aesar (Ward Hill, MA, USA). Bovine serum albumin (BSA) was purchased from VWR International, LLC (Solon, OH, USA). Recombinant bovine interferon-gamma (IFN-γ) (Cat. No. PBP001), recombinant bovine interleukin-10 (IL-10) (Cat. No. PBP016A), mouse anti-bovine interferon-gamma (anti IFN-γ) (mAb, Cat. No. MCA1783), and mouse anti-bovine interleukin-10 (anti IL-10) (mAb, Cat. No. MCA2110) were purchased from Bio-Rad Laboratories Inc. (Hercules, CA, USA). All solutions were prepared in phosphate-buffered saline (1× PBS) buffer.

The bovine implant was acquired by a stainless-steel implant device with a window that was placed in the subcutis of the cattle. A collagen plug was extracted from the subcutis, surrounded by a nylon mesh with a pore size of 30 μm. The extracted bovine implant was minced and centrifuged at 1000 rpm for 30 min. The collected supernatant was diluted (1:1000) and further used for sensing IFN-γ and IL-10.

4.1. Graphene-Nitrocellulose Powder and Ink Preparation. Graphene-nitrocellulose powder was prepared as in our previous work.[50] Briefly, a 1:1 mixture of graphite powder and nitrocellulose in acetone was exfoliated via shear mixing for 4 h at 10230 rpm. The product was centrifuged in two steps, 5000 rpm for 15 min and 6000 rpm for 20 min, and the resultant supernatant was collected. The graphene-nitrocellulose supernatant was flocculated with NaCl and centrifuged to form a pellet. The pellet was washed with DI water and then collected on a membrane using vacuum filtration. The product was collected, dried, and crushed with a mortar and pestle into a fine powder. This graphene-nitrocellulose powder was then dispersed via bath ultrasonication in a 1:9 v/v mixture of dibutyl phthalate and ethyl lactate, for a total solid loading of 30 mg/mL. The total sonication time was 6 h.

4.2. Aerosol Jet Printing of Interdigitated Electrodes. The graphene-nitrocellulose ink was aerosol jet printed (Optomec, AJ 200) to form IDE patterns on a Kapton substrate that was heated to 60 °C in air during printing. Sheath flow rates were in the range of 40−60 sccm, and carrier flow rates were in the range of 15−45 sccm. Printing speed was maintained at 5 mm/s. After printing, the devices were heat-treated in a tube furnace (Thermo Scientific, Lindberg Blue M) at 350 °C in air at atmospheric pressure for 30 min to decompose nitrocellulose into a conductive carbon residue.[50]

4.3. Biofunctionalization of Graphene IDE. The printed graphene IDE was annealed in a CO_2 environment at 400 °C for 2 h in an OTF-1200X tube furnace (MTI Corporation, Richmond, CA, USA) to increase the quantity of surface carboxyl functional groups on the graphene. Next, the IDE was functionalized using 0.4 M EDC and 0.1 M NHS in 0.1 M MES buffer for 1 h at room temperature followed by an overnight incubation in either (1:50) mouse anti-bovine IFN-γ or IL-10 solution. The unreacted EDC/NHS on the graphene IDE was quenched using 1 M ethanolamine for 20 min, and the exposed, unfunctionalized portion of the IDE surface was blocked using a mixture of 0.1% Tween-20, 0.1% fish gelatin, and 1% BSA for 1 h in an effort to prevent nonspecific adsorption of nontarget analytes.[65] Before subsequent biosensing experiments, a baseline electrochemical impedance spectrum was acquired over the frequency range of 0.1 Hz−100 kHz with a voltage amplitude of 10 mV using a 5 mM ferro/ferricyanide (1:1) redox probe. Next, the graphene IDE was incubated with 100 μL of test solution containing IFN-γ or IL-10 (prepared in bovine minced implant serum) for 30 min to allow the IFN-γ or IL-10 to bind to the immobilized antibody on the graphene IDE surface. After a baseline EIS measurement was obtained, calibration plots were obtained by measuring R_{ct} for successively increasing concentrations of the IFN-γ or IL-10 target analyte.

4.4. Confocal Laser Microscopy. Three-dimensional height profiles of printed graphene lines were obtained via confocal laser microscopy using an Olympus OLS5000 laser confocal microscope. Data was collected at the 50× objective, which enables a lateral resolution of 200 nm and a vertical resolution of 6 nm. All data analysis was performed in the Olympus software.

4.5. Atomic Force Microscopy. Thickness measurements of the printed graphene IDE were performed using noncontact-mode atomic force microscopy (Asylum Research Cypher AFM). The graphene IDEs were printed on Kapton for AFM measurements.

4.6. Scanning Electron Microscopy. SEM images of the printed graphene IDEs were obtained using an LEO Gemini 1525 SEM and Hitachi SU8030 SEM. A 10 nm layer of osmium was coated on printed samples to prevent charging effects with the nonconductive Kapton.

4.7. X-ray Photoelectron Spectroscopy. The XPS measurements were performed using a Kratos Amicus/ESCA 3400 instrument. The sample was irradiated with 240 W unmonochromated Al Kα X-rays, and photoelectrons emitted at 0° from the surface normal were energy-analyzed using a DuPont type analyzer. The pass energy was set at 150 eV, and a Shirley baseline was removed from all reported spectra. CasaXPS was used to process raw data files.

4.8. Raman Spectroscopy. Raman spectroscopy measurements were performed using an XploRa Plus confocal Raman upright microscope, equipped with a 785 nm laser excitation source (5 mW at the sample) and a Synapse EMCCD camera (Horiba Scientific/JY, France). A 100× air objective (Olympus, LMPlanFL) with a 0.9 numerical aperture was used to collect the Raman signal under ambient laboratory conditions. The spectra were collected from 1000 to 3300 cm^{-1} with a 600 grooves/mm grating. Reported spectra were an average of three measurements, with a 30 s acquisition time for

https://dx.doi.org/10.1021/acsami.9b22183
ACS Appl. Mater. Interfaces 2020, 12, 8592−8603

each spectrum. All data were processed using Igor Pro 6.37 scientific analysis and graphing software (Wavemetrics, Lake Oswego, OR, USA). The spectra were fitted to a Lorentzian function with a linear baseline using the multifit peak function in order to extract the peak intensity (height).

■ ASSOCIATED CONTENT

Supporting Information

The Supporting Information is available free of charge at https://pubs.acs.org/doi/10.1021/acsami.9b22183.

Demonstration of tunable film thickness with printing parameters, SEM images to demonstrate the influence of printed graphene porosity on electrical properties, printed graphene film thickness characterization on Kapton using confocal laser microscopy, analysis of material consumption during printing with a table comparing printed line properties, and optimization of blocking agent for biofunctionalization of graphene IDE (PDF)

■ AUTHOR INFORMATION

Corresponding Authors

Mark C. Hersam − *Department of Materials Science & Engineering, Northwestern University, Evanston, Illinois 60208, United States;* orcid.org/0000-0003-4120-1426; Email: m-hersam@northwestern.edu

Jonathan C. Claussen − *Department of Mechanical Engineering, Iowa State University, Ames, Iowa 50011, United States;* orcid.org/0000-0001-7065-1077; Email: jcclauss@iastate.edu

Authors

Kshama Parate − *Department of Mechanical Engineering, Iowa State University, Ames, Iowa 50011, United States*

Sonal V. Rangnekar − *Department of Materials Science & Engineering, Northwestern University, Evanston, Illinois 60208, United States*

Dapeng Jing − *Materials Analysis and Research Laboratory, Iowa State University, Ames, Iowa 50010, Unites States;* orcid.org/0000-0001-7600-7071

Deyny L. Mendivelso-Perez − *Department of Chemistry, Iowa State University, Ames, Iowa 50011, United States;* orcid.org/0000-0001-8261-5081

Shaowei Ding − *Department of Mechanical Engineering, Iowa State University, Ames, Iowa 50011, United States*

Ethan B. Secor − *Department of Materials Science & Engineering, Northwestern University, Evanston, Illinois 60208, United States*

Emily A. Smith − *Department of Chemistry, Iowa State University, Ames, Iowa 50011, United States*

Jesse M. Hostetter − *College of Veterinary Medicine, Iowa State University, Ames, Iowa 50011, United States*

Complete contact information is available at: https://pubs.acs.org/10.1021/acsami.9b22183

Author Contributions

‡K.P. and S.V.R. contributed equally to this work.

Notes

The authors declare no competing financial interest.

■ ACKNOWLEDGMENTS

J.C.C. gratefully acknowledges funding support for this work from the National Science Foundation under award number CBET-1706994 and ECCS-1841649 as well as from the U.S. Department of Agriculture, under award number 2016-67021-25038. J.M.H. acknowledges funding support from the Iowa Veterinary Medical Association and Iowa Livestock Health Advisory Council. E.B.S. was supported by the Air Force Research Laboratory under agreement number FA8650-15-2-5518. S.V.R. was supported by the U.S. Department of Commerce, National Institute of Standards and Technology (Award 70NANB19H005) as part of the Center for Hierarchical Materials Design (CHiMaD). This work made use of the EPIC Facility of Northwestern University's NUANCE Center, which has received support from the Soft and Hybrid Nanotechnology Experimental (SHyNE) Resource (NSF ECCS-1542205); the MRSEC program (NSF DMR-1720139) at the Materials Research Center; the International Institute for Nanotechnology (IIN); the Keck Foundation; and the State of Illinois, through the IIN. The U.S. Government is authorized to reproduce and distribute reprints for Governmental purposes notwithstanding any copyright notation thereon. The views and conclusions contained herein are those of the authors and should not be interpreted as necessarily representing the official policies or endorsements, either expressed or implied, of the sponsors.

■ REFERENCES

(1) Hondred, J. A.; Stromberg, L. R.; Mosher, C. L.; Claussen, J. C. High-Resolution Graphene Films for Electrochemical Sensing Via Inkjet Maskless Lithography. *ACS Nano* **2017**, *11*, 9836−9845.

(2) Hyun, W. J.; Secor, E. B.; Hersam, M. C.; Frisbie, C. D.; Francis, L. F. High-Resolution Patterning of Graphene by Screen Printing with a Silicon Stencil for Highly Flexible Printed Electronics. *Adv. Mater.* **2015**, *27*, 109−115.

(3) Bandodkar, A. J.; Jeerapan, I.; You, J.-M.; Nuñez-Flores, R.; Wang, J. Highly Stretchable Fully-Printed Cnt-Based Electrochemical Sensors and Biofuel Cells: Combining Intrinsic and Design-Induced Stretchability. *Nano Lett.* **2015**, *16*, 721−727.

(4) Chen, B.; Kruse, M.; Xu, B.; Tutika, R.; Zheng, W.; Bartlett, M. D.; Wu, Y.; Claussen, J. C. Flexible Thermoelectric Generators with Inkjet-Printed Bismuth Telluride Nanowires and Liquid Metal Contacts. *Nanoscale* **2019**, *11*, 5222−5230.

(5) Honda, W.; Harada, S.; Arie, T.; Akita, S.; Takei, K. Wearable, Human-Interactive, Health-Monitoring, Wireless Devices Fabricated by Macroscale Printing Techniques. *Adv. Funct. Mater.* **2014**, *24*, 3299−3304.

(6) Lorwongtragool, P.; Sowade, E.; Watthanawisuth, N.; Baumann, R.; Kerdcharoen, T. A Novel Wearable Electronic Nose for Healthcare Based on Flexible Printed Chemical Sensor Array. *Sensors* **2014**, *14*, 19700−19712.

(7) Núñez, C. G.; Manjakkal, L.; Dahiya, R. Energy Autonomous Electronic Skin. *npj Flexible Electron* **2019**, *3*, 1−24.

(8) Sundriyal, P.; Bhattacharya, S. Inkjet-Printed Electrodes on A4 Paper Substrates for Low-Cost, Disposable, and Flexible Asymmetric Supercapacitors. *ACS Appl. Mater. Interfaces* **2017**, *9*, 38507−38521.

(9) Zhang, C.; McKeon, L.; Kremer, M. P.; Park, S.-H.; Ronan, O.; Seral-Ascaso, A.; Barwich, S.; Coileáin, C. Ó.; McEvoy, N.; Nerl, H. C.; Anasori, B.; Coleman, J. N.; Gogotsi, Y.; Nicolosi, V. Additive-Free Mxene Inks and Direct Printing of Micro-Supercapacitors. *Nat. Commun* **2019**, *10*, 1795.

(10) Das, S. R.; Nian, Q.; Cargill, A. A.; Hondred, J. A.; Ding, S.; Saei, M.; Cheng, G. J.; Claussen, J. C. 3d Nanostructured Inkjet Printed Graphene Via Uv-Pulsed Laser Irradiation Enables Paper-Based Electronics and Electrochemical Devices. *Nanoscale* **2016**, *8*, 15870−15879.

(11) Huang, L.; Huang, Y.; Liang, J.; Wan, X.; Chen, Y. Graphene-Based Conducting Inks for Direct Inkjet Printing of Flexible Conductive Patterns and Their Applications in Electric Circuits and Chemical Sensors. *Nano Res.* **2011**, *4*, 675−684.
(12) Yu, H. K.; Balasubramanian, K.; Kim, K.; Lee, J.-L.; Maiti, M.; Ropers, C.; Krieg, J.; Kern, K.; Wodtke, A. M. Chemical Vapor Deposition of Graphene on a "Peeled-Off" Epitaxial Cu (111) Foil: A Simple Approach to Improved Properties. *ACS Nano* **2014**, *8*, 8636−8643.
(13) Gomez De Arco, L.; Zhang, Y.; Schlenker, C. W.; Ryu, K.; Thompson, M. E.; Zhou, C. Continuous, Highly Flexible, and Transparent Graphene Films by Chemical Vapor Deposition for Organic Photovoltaics. *ACS Nano* **2010**, *4*, 2865−2873.
(14) Hernandez, Y.; Nicolosi, V.; Lotya, M.; Blighe, F. M.; Sun, Z.; De, S.; McGovern, I. T.; Holland, B.; Byrne, M.; Gun'Ko, Y. K.; et al. High-Yield Production of Graphene by Liquid-Phase Exfoliation of Graphite. *Nat. Nanotechnol.* **2008**, *3*, 563.
(15) Krebs, F. C.; Fyenbo, J.; Jørgensen, M. Product Integration of Compact Roll-to-Roll Processed Polymer Solar Cell Modules: Methods and Manufacture Using Flexographic Printing, Slot-Die Coating and Rotary Screen Printing. *J. Mater. Chem.* **2010**, *20*, 8994.
(16) Secor, E. B.; Prabhumirashi, P. L.; Puntambekar, K.; Geier, M. L.; Hersam, M. C. Inkjet Printing of High Conductivity, Flexible Graphene Patterns. *J. Phys. Chem. Lett.* **2013**, *4*, 1347−1351.
(17) Lamas-Ardisana, P. J.; Martínez-Paredes, G.; Añorga, L.; Grande, H. J. Glucose Biosensor Based on Disposable Electrochemical Paper-Based Transducers Fully Fabricated by Screen-Printing. *Biosens. Bioelectron.* **2018**, *109*, 8−12.
(18) Song, D.; Mahajan, A.; Secor, E. B.; Hersam, M. C.; Francis, L. F.; Frisbie, C. D. High-Resolution Transfer Printing of Graphene Lines for Fully Printed, Flexible Electronics. *ACS Nano* **2017**, *11*, 7431−7439.
(19) Hondred, J. A.; Breger, J. C.; Alves, N. J.; Trammell, S. A.; Walper, S. A.; Medintz, I. L.; Claussen, J. C. Printed Graphene Electrochemical Biosensors Fabricated by Inkjet Maskless Lithography for Rapid and Sensitive Detection of Organophosphates. *ACS Appl. Mater. Interfaces* **2018**, *10*, 11125−11134.
(20) He, Q.; Das, S. R.; Garland, N. T.; Jing, D.; Hondred, J. A.; Cargill, A. A.; Ding, S.; Karunakaran, C.; Claussen, J. C. Enabling Inkjet Printed Graphene for Ion Selective Electrodes with Postprint Thermal Annealing. *ACS Appl. Mater. Interfaces* **2017**, *9*, 12719−12727.
(21) Ding, S.; Das, S. R.; Brownlee, B. J.; Parate, K.; Davis, T. M.; Stromberg, L. R.; Chan, E. K. L.; Katz, J.; Iverson, B. D.; Claussen, J. C. Cip2a Immunosensor Comprised of Vertically-Aligned Carbon Nanotube Interdigitated Electrodes Towards Point-of-Care Oral Cancer Screening. *Biosens. Bioelectron* **2018**, 68.
(22) Ding, S.; Mosher, C.; Lee, X. Y.; Das, S. R.; Cargill, A. A.; Tang, X.; Chen, B.; McLamore, E. S.; Gomes, C.; Hostetter, J. M.; Claussen, J. C. Rapid and Label-Free Detection of Interferon Gamma Via an Electrochemical Aptasensor Comprising a Ternary Surface Monolayer on a Gold Interdigitated Electrode Array. *ACS Sens.* **2017**, *2*, 210−217.
(23) van Gerwen, P.; Laureyn, W.; Laureys, W.; Huyberechts, G.; de Beeck, M. O.; Baert, K.; Suls, J.; Sansen, W.; Jacobs, P.; Hermans, L.; Mertens, R. Nanoscaled Interdigitated Electrode Arrays for Biochemical Sensors. *Sens. Actuators, B* **1998**, *49*, 73−80.
(24) Ko, S. H.; Pan, H.; Grigoropoulos, C. P.; Luscombe, C. K.; Fréchet, J. M. J.; Poulikakos, D. All-Inkjet-Printed Flexible Electronics Fabrication on a Polymer Substrate by Low-Temperature High-Resolution Selective Laser Sintering of Metal Nanoparticles. *Nanotechnology* **2007**, *18*, 345202.
(25) Shimoni, A.; Azoubel, S.; Magdassi, S. Inkjet Printing of Flexible High-Performance Carbon Nanotube Transparent Conductive Films by "Coffee Ring Effect". *Nanoscale* **2014**, *6*, 11084−11089.
(26) Zhang, L.; Liu, H.; Zhao, Y.; Sun, X.; Wen, Y.; Guo, Y.; Gao, X.; Di, C.-a.; Yu, G.; Liu, Y. Inkjet Printing High-Resolution, Large-Area Graphene Patterns by Coffee-Ring Lithography. *Adv. Mater.* **2012**, *24*, 436−440.
(27) Zhang, Z.; Zhang, X.; Xin, Z.; Deng, M.; Wen, Y.; Song, Y. Controlled Inkjetting of a Conductive Pattern of Silver Nanoparticles Based on the Coffee-Ring Effect. *Adv. Mater.* **2013**, *25*, 6714−6718.
(28) Jabari, E.; Toyserkani, E. Micro-Scale Aerosol-Jet Printing of Graphene Interconnects. *Carbon* **2015**, *91*, 321−329.
(29) Secor, E. B. Principles of Aerosol Jet Printing. *Flex. Print. Electron.* **2018**, *3*, No. 035002.
(30) Cai, F.; Chang, Y.-h.; Wang, K.; Khan, W. T.; Pavlidis, S. Papapolymerou, J. In *High Resolution Aerosol Jet Printing of D-Band Printed Transmission Lines on Flexible Lcp Substrate 2014* IEEE MTT-S International Microwave Symposium (IMS2014), *IEEE*: 2014; pp 1−3.
(31) Mahajan, A.; Frisbie, C. D.; Francis, L. F. Optimization of Aerosol Jet Printing for High-Resolution, High-Aspect Ratio Silver Lines. *ACS Appl. Mater. Interfaces* **2013**, *5*, 4856−4864.
(32) Deiner, L. J.; Reitz, T. L. Inkjet and Aerosol Jet Printing of Electrochemical Devices for Energy Conversion and Storage. *Adv. Eng. Mater.* **2017**, *19*, 1600878.
(33) Akedo, J. In *Aerosol Deposition Method for Fabrication of Nano Crystal Ceramic Layer*; Materials Science Forum, Trans Tech Publ: 2004; pp 43−48.
(34) Ha, M.; Seo, J.-W. T.; Prabhumirashi, P. L.; Zhang, W.; Geier, M. L.; Renn, M. J.; Kim, C. H.; Hersam, M. C.; Frisbie, C. D. Aerosol Jet Printed, Low Voltage, Electrolyte Gated Carbon Nanotube Ring Oscillators with Sub-5 Ms Stage Delays. *Nano Lett.* **2013**, *13*, 954−960.
(35) Kim, S. H.; Hong, K.; Lee, K. H.; Frisbie, C. D. Performance and Stability of Aerosol-Jet-Printed Electrolyte-Gated Transistors Based on Poly (3-Hexylthiophene). *ACS Appl. Mater. Interfaces* **2013**, *5*, 6580−6585.
(36) Pandhi, T.; Kreit, E.; Aga, R.; Fujimoto, K.; Sharbati, M. T.; Khademi, S.; Chang, A. N.; Xiong, F.; Koehne, J.; Heckman, E. M.; Estrada, D. Electrical Transport and Power Dissipation in Aerosol-Jet-Printed Graphene Interconnects. *Sci. Rep.* **2018**, *8*, 10842.
(37) Bodini, A.; Serpelloni, M.; Sardini, E.; Tonello, S. In Design and Implementation of a Microsensor Platform for Protein Detection Realized Via 3-D Printing, *2018 IEEE Sensors Applications Symposium (SAS)*, IEEE: 2018; pp 1−6.
(38) Grunwald, I.; Groth, E.; Wirth, I.; Schumacher, J.; Maiwald, M.; Zoellmer, V.; Busse, M. Surface Biofunctionalization and Production of Miniaturized Sensor Structures Using Aerosol Printing Technologies. *Biofabrication* **2010**, *2*, No. 014106.
(39) Marziano, M.; Tonello, S.; Cantù, E.; Abate, G.; Vezzoli, M.; Rungratanawanich, W.; Serpelloni, M.; Lopomo, N. F.; Memo, M.; Sardini, E.; Uberti, D. Monitoring Caco-2 to Enterocyte-Like Cells Differentiation by Means of Electric Impedance Analysis on Printed Sensors. *Biochim. Biophys. Acta, Gen. Subj.* **2019**, *1863*, 893−902.
(40) Ye, R.; James, D. K.; Tour, J. M. Laser-Induced Graphene. *Acc. Chem. Res.* **2018**, *51*, 1609−1620.
(41) Conti-Freitas, L. C.; Foss-Freitas, M. C.; Mamede, R.; Foss, N. T. Interferon-Gamma and Interleukin-10 Production by Mononuclear Cells from Patients with Advanced Head and Neck Cancer. *Clinics* **2012**, *67*, 587−590.
(42) Yin, Z.; Siegert, S.; Neure, L.; Grolms, M.; Liu, L.; Eggens, U.; Radbruch, A.; Braun, J.; Sieper, J. The Elevated Ratio of Interferon Gamma−/ Interleukin-4-Positive T Cells Found in Synovial Fluid and Synovial Membrane of Rheumatoid Arthritis Patients Can Be Changed by Interleukin-4 but Not by Interleukin-10 or Transforming Growth Factor Beta. *Rheumatology* **1999**, *38*, 1058−1067.
(43) Skolimowska, K. H.; Rangaka, M. X.; Meintjes, G.; Pepper, D. J.; Seldon, R.; Matthews, K.; Wilkinson, R. J.; Wilkinson, K. A. Altered Ratio of IFN-γ/IL-10 in Patients with Drug Resistant Mycobacterium tuberculosis and HIV- Tuberculosis Immune Reconstitution Inflammatory Syndrome. *PLoS One* **2012**, *7*, No. e46481.
(44) Khalifeh, M. S.; Stabel, J. R. Effects of Gamma Interferon, Interleukin-10, and Transforming Growth Factor on the Survival of Mycobacterium Avium Subsp. Paratuberculosis in Monocyte-Derived

https://dx.doi.org/10.1021/acsami.9b22183
ACS Appl. Mater. Interfaces 2020, 12, 8592−8603

Macrophages from Naturally Infected Cattle. *Infect. Immun.* **2004**, *72*, 1974−1982.
(45) Khalifeh, M. S.; Stabel, J. R. Upregulation of Transforming Growth Factor-Beta and Interleukin-10 in Cows with Clinical Johne's Disease. *Vet. Immunol. Immunopathol.* **2004**, *99*, 39−46.
(46) López-Maderuelo, D.; Arnalich, F.; Serantes, R.; González, A.; Codoceo, R.; Madero, R.; Vázquez, J. J.; Montiel, C. Interferon-Γ and Interleukin-10 Gene Polymorphisms in Pulmonary Tuberculosis. *Am. J. Respir. Crit. Care Med.* **2003**, *167*, 970−975.
(47) Piazzolla, G.; Tortorella, C.; Schiraldi, O.; Antonaci, S. Relationship between Interferon-Γ, Interleukin-10, and Interleukin-12 Production in Chronic Hepatitis C and in Vitro Effects of Interferon-A. *J. Clin. Immunol.* **2000**, *20*, 54−61.
(48) Bjerre, A.; Brusletto, B.; Høiby, E. A.; Kierulf, P.; Brandtzaeg, P. Plasma Interferon-Γ and Interleukin-10 Concentrations in Systemic Meningococcal Disease Compared with Severe Systemic Gram-Positive Septic Shock. *Crit. Care Med.* **2004**, *32*, 433−438.
(49) Secor, E. B.; Cook, A. B.; Tabor, C. E.; Hersam, M. C. Wiring up Liquid Metal: Stable and Robust Electrical Contacts Enabled by Printable Graphene Inks. *Adv. Electron. Mater.* **2018**, *4*, 1700483.
(50) Secor, E. B.; Gao, T. Z.; Islam, A. E.; Rao, R.; Wallace, S. G.; Zhu, J.; Putz, K. W.; Maruyama, B.; Hersam, M. C. Enhanced Conductivity, Adhesion, and Environmental Stability of Printed Graphene Inks with Nitrocellulose. *Chem. Mater.* **2017**, *29*, 2332−2340.
(51) Qu, J.; He, N.; Patil, S. V.; Wang, Y.; Banerjee, D.; Gao, W. Screen Printing of Graphene Oxide Patterns onto Viscose Nonwovens with Tunable Penetration Depth and Electrical Conductivity. *ACS Appl. Mater. Interfaces* **2019**, *11*, 14944−14951.
(52) Sui, Y.; Hess-Dunning, A.; Wei, P.; Pentzer, E.; Sankaran, R. M.; Zorman, C. A. Electrically Conductive, Reduced Graphene Oxide Structures Fabricated by Inkjet Printing and Low Temperature Plasma Reduction. *Adv. Mater. Technol.* **2019**, 1900834.
(53) Majee, S.; Song, M.; Zhang, S.-L.; Zhang, Z.-B. Scalable Inkjet Printing of Shear-Exfoliated Graphene Transparent Conductive Films. *Carbon* **2016**, *102*, 51−57.
(54) Ferrari, A. C.; Meyer, J. C.; Scardaci, V.; Casiraghi, C.; Lazzeri, M.; Mauri, F.; Piscanec, S.; Jiang, D.; Novoselov, K. S.; Roth, S.; Geim, A. K. Raman Spectrum of Graphene and Graphene Layers. *Phys. Rev. Lett.* **2006**, *97*, 187401.
(55) Stankovich, S.; Dikin, D. A.; Piner, R. D.; Kohlhaas, K. A.; Kleinhammes, A.; Jia, Y.; Wu, Y.; Nguyen, S. T.; Ruoff, R. S. Synthesis of Graphene-Based Nanosheets Via Chemical Reduction of Exfoliated Graphite Oxide. *Carbon* **2007**, *45*, 1558−1565.
(56) Yang, D.; Velamakanni, A.; Bozoklu, G.; Park, S.; Stoller, M.; Piner, R. D.; Stankovich, S.; Jung, I.; Field, D. A.; Ventrice, C. A., Jr.; Ruoff, R. S. Chemical Analysis of Graphene Oxide Films after Heat and Chemical Treatments by X-Ray Photoelectron and Micro-Raman Spectroscopy. *Carbon* **2009**, *47*, 145−152.
(57) Pimenta, M. A.; Dresselhaus, G.; Dresselhaus, M. S.; Cançado, L. G.; Jorio, A.; Saito, R. Studying Disorder in Graphite-Based Systems by Raman Spectroscopy. *Phys. Chem. Chem. Phys.* **2007**, *9*, 1276−1290.
(58) Childres, I.; Jauregui, L. A.; Park, W.; Cao, H.; Chen, Y. P. *Raman Spectroscopy of Graphene and Related Materials*; 2013; Vol. *1*.
(59) Torrisi, F.; Hasan, T.; Wu, W.; Sun, Z.; Lombardo, A.; Kulmala, T. S.; Hsieh, G.-W.; Jung, S.; Bonaccorso, F.; Paul, P. J.; Chu, D.; Ferrari, A. C. Inkjet-Printed Graphene Electronics. *ACS Nano* **2012**, *6*, 2992−3006.
(60) Karuppiah, C.; Cheemalapati, S.; Chen, S.-M.; Palanisamy, S. Carboxyl-Functionalized Graphene Oxide-Modified Electrode for the Electrochemical Determination of Nonsteroidal Anti-Inflammatory Drug Diclofenac. *Ionics* **2015**, *21*, 231−238.
(61) Ambrosi, A.; Chua, C. K.; Bonanni, A.; Pumera, M. Electrochemistry of Graphene and Related Materials. *Chem. Rev.* **2014**, *114*, 7150−7188.
(62) Ambrosi, A.; Pumera, M. Electrochemistry at Cvd Grown Multilayer Graphene Transferred onto Flexible Substrates. *J. Phys. Chem. C* **2013**, *117*, 2053−2058.
(63) Pope, M. A.; Punckt, C.; Aksay, I. A. Intrinsic Capacitance and Redox Activity of Functionalized Graphene Sheets. *J. Phys. Chem. C* **2011**, *115*, 20326−20334.
(64) Bard, A. J.; Faulkner, L. R. *Electrochemical Methods: Fundamentals and Applications*; Wiley New york: NY, USA, 2001.
(65) Mao, S.; Yu, K.; Lu, G.; Chen, J. Highly Sensitive Protein Sensor Based on Thermally-Reduced Graphene Oxide Field-Effect Transistor. *Nano Res.* **2011**, *4*, 921.
(66) Yang, F.; Han, J.; Zhuo, Y.; Yang, Z.; Chai, Y.; Yuan, R. Highly Sensitive Impedimetric Immunosensor Based on Single-Walled Carbon Nanohorns as Labels and Bienzyme Biocatalyzed Precipitation as Enhancer for Cancer Biomarker Detection. *Biosens. Bioelectron.* **2014**, *55*, 360−365.
(67) Lago, P. M.; Boéchat, N.; Migueis, D. P.; Almeida, A. S.; Lazzarini, L. C.; Saldanha, M. M.; Kritski, A. L.; Ho, J. L.; Lapa e Silva, J. R. Interleukin-10 and Interferon-Gamma Patterns During Tuberculosis Treatment: Possible Association with Recurrence. *Int. J. Tuberc. Lung Dis.* **2012**, *16*, 656−659.
(68) Zdanov, A.; Schalk-Hihi, C.; Gustchina, A.; Tsang, M.; Weatherbee, J.; Wlodawer, A. Crystal Structure of Interleukin-10 Reveals the Functional Dimer with an Unexpected Topological Similarity to Interferon Γ. *Structure* **1995**, *3*, 591−601.
(69) Lai, C.-F.; Ripperger, J.; Morella, K. K.; Jurlander, J.; Hawley, T. S.; Carson, W. E.; Kordula, T.; Caligiuri, M. A.; Hawley, R. G.; Fey, G. H.; Baumann, H. Receptors for Interleukin (Il)-10 and Il-6-Type Cytokines Use Similar Signaling Mechanisms for Inducing Transcription through Il-6 Response Elements. *J. Biol. Chem.* **1996**, *271*, 13968−13975.
(70) Plattner, B. L.; Huffman, E. L.; Hostetter, J. M. Gamma-Delta T-Cell Responses During Subcutaneous Mycobacterium Avium Subspecies Paratuberculosis Challenge in Sensitized or Naive Calves Using Matrix Biopolymers. *Vet. Pathol.* **2013**, *50*, 630−637.
(71) Szodoray, P.; Alex, P.; Brun, J. G.; Centola, M.; Jonsson, R. Circulating Cytokines in Primary Sjögren's Syndrome Determined by a Multiplex Cytokine Array System. *Scand. J. Immunol.* **2004**, *59*, 592−599.
(72) Zhang, B.; Price, J.; Hong, G.; Tabakman, S. M.; Wang, H.; Jarrell, J. A.; Feng, J.; Utz, P. J.; Dai, H. Multiplexed Cytokine Detection on Plasmonic Gold Substrates with Enhanced near-Infrared Fluorescence. *Nano Res.* **2012**, *6*, 113−120.
(73) Ooi, K. G.-J.; Galatowicz, G.; Towler, H. M. A.; Lightman, S. L.; Calder, V. L. Multiplex Cytokine Detection Versus Elisa for Aqueous Humor: Il-5, Il-10, and Ifnγ Profiles in Uveitis. *Invest. Ophthalmology Visual Sci.* **2006**, *47*, 272−277.
(74) Fairchild, A. B.; McAferty, K.; Demirok, U. K.; La Belle, J. T. In A Label-Free, Rapid Multimarker Protein Impedance-Based Immunosensor, *Complex Medical Engineering, 2009. CME. ICME International Conference on*, IEEE: 2009; pp 1−5.
(75) Du, D.; Zou, Z.; Shin, Y.; Wang, J.; Wu, H.; Engelhard, M. H.; Liu, J.; Aksay, I. A.; Lin, Y. Sensitive Immunosensor for Cancer Biomarker Based on Dual Signal Amplification Strategy of Graphene Sheets and Multienzyme Functionalized Carbon Nanospheres. *Anal. Chem.* **2010**, *82*, 2989−2995.
(76) Carinelli, S.; Martí, M.; Alegret, S.; Pividori, M. I. Biomarker Detection of Global Infectious Diseases Based on Magnetic Particles. *New Biotechnol.* **2015**, *32*, 521−532.
(77) Viswanathan, S.; Rani, C.; Ho, J.-A. A. Electrochemical Immunosensor for Multiplexed Detection of Food-Borne Pathogens Using Nanocrystal Bioconjugates and Mwcnt Screen-Printed Electrode. *Talanta* **2012**, *94*, 315−319.
(78) Hyun, W. J.; Secor, E. B.; Rojas, G. A.; Hersam, M. C.; Francis, L. F.; Frisbie, C. D. All-Printed, Foldable Organic Thin-Film Transistors on Glassine Paper. *Adv. Mater.* **2015**, *27*, 7058−7064.
(79) El-Kady, M. F.; Shao, Y.; Kaner, R. B. Graphene for Batteries, Supercapacitors and Beyond. *Nat. Rev. Mater.* **2016**, *1*, 16033.
(80) Raccichini, R.; Varzi, A.; Passerini, S.; Scrosati, B. The Role of Graphene for Electrochemical Energy Storage. *Nat. Mater.* **2015**, *14*, 271.

https://dx.doi.org/10.1021/acsami.9b22183
ACS Appl. Mater. Interfaces 2020, 12, 8592−8603

(81) Shao, Y.; El-Kady, M. F.; Lin, C. W.; Zhu, G.; Marsh, K. L.; Hwang, J. Y.; Zhang, Q.; Li, Y.; Wang, H.; Kaner, R. B. 3d Freeze-Casting of Cellular Graphene Films for Ultrahigh-Power-Density Supercapacitors. *Adv. Mater.* **2016**, *28*, 6719−6726.
(82) Yang, J.; Gunasekaran, S. Electrochemically Reduced Graphene Oxide Sheets for Use in High Performance Supercapacitors. *Carbon* **2013**, *51*, 36−44.
(83) Xiong, G.; He, P.; Huang, B.; Chen, T.; Bo, Z.; Fisher, T. S. Graphene Nanopetal Wire Supercapacitors with High Energy Density and Thermal Durability. *Nano Energy* **2017**, *38*, 127−136.
(84) Koushanpour, A.; Guz, N.; Gamella, M.; Katz, E. Biofuel Cell Based on Carbon Fiber Electrodes Functionalized with Graphene Nanosheets. *ECS J. Solid State Sci. Technol.* **2016**, *5*, M3037−M3040.
(85) Xiao, L.; Damien, J.; Luo, J.; Jang, H. D.; Huang, J.; He, Z. Crumpled Graphene Particles for Microbial Fuel Cell Electrodes. *J. Power Sources* **2012**, *208*, 187−192.
(86) Gao, W.; Emaminejad, S.; Nyein, H. Y. Y.; Challa, S.; Chen, K.; Peck, A.; Fahad, H. M.; Ota, H.; Shiraki, H.; Kiriya, D.; Lien, D.-H.; Brooks, G. A.; Davis, R. W.; Javey, A. Fully Integrated Wearable Sensor Arrays for Multiplexed in Situ Perspiration Analysis. *Nature* **2016**, *529*, 509.
(87) Imani, S.; Bandodkar, A. J.; Mohan, A. M. V.; Kumar, R.; Yu, S.; Wang, J.; Mercier, P. P. A Wearable Chemical−Electrophysiological Hybrid Biosensing System for Real-Time Health and Fitness Monitoring. *Nat. Commun.* **2016**, *7*, 11650.
(88) Kim, J.; Campbell, A. S.; de Ávila, B. E.-F.; Wang, J. Wearable Biosensors for Healthcare Monitoring. *Nat. Biotechnol.* **2019**, *37*, 389.
(89) Han, T.-H.; Lee, Y.; Choi, M.-R.; Woo, S.-H.; Bae, S.-H.; Hong, B. H.; Ahn, J.-H.; Lee, T.-W. Extremely Efficient Flexible Organic Light-Emitting Diodes with Modified Graphene Anode. *Nat. Photonics* **2012**, *6*, 105.
(90) Park, H.; Chang, S.; Zhou, X.; Kong, J.; Palacios, T.; Gradečak, S. Flexible Graphene Electrode-Based Organic Photovoltaics with Record-High Efficiency. *Nano Lett.* **2014**, *14*, 5148−5154.
(91) Tian, H.; Shu, Y.; Cui, Y.-L.; Mi, W.-T.; Yang, Y.; Xie, D.; Ren, T.-L. Scalable Fabrication of High-Performance and Flexible Graphene Strain Sensors. *Nanoscale* **2014**, *6*, 699−705.
(92) Kim, J.; de Araujo, W. R.; Samek, I. A.; Bandodkar, A. J.; Jia, W.; Brunetti, B.; Paixão, T. R. L. C.; Wang, J. Wearable Temporary Tattoo Sensor for Real-Time Trace Metal Monitoring in Human Sweat. *Electrochem. Commun* **2015**, *51*, 41−45.
(93) Mannoor, M. S.; Tao, H.; Clayton, J. D.; Sengupta, A.; Kaplan, D. L.; Naik, R. R.; Verma, N.; Omenetto, F. G.; McAlpine, M. C. Graphene-Based Wireless Bacteria Detection on Tooth Enamel. *Nat. Commun* **2012**, *3*, 763.
(94) Sonner, Z.; Wilder, E.; Heikenfeld, J.; Kasting, G.; Beyette, F.; Swaile, D.; Sherman, F.; Joyce, J.; Hagen, J.; Kelley-Loughnane, N.; Naik, R. The Microfluidics of the Eccrine Sweat Gland, Including Biomarker Partitioning, Transport, and Biosensing Implications. *Biomicrofluidics* **2015**, *9*, No. 031301.

https://dx.doi.org/10.1021/acsami.9b22183
ACS Appl. Mater. Interfaces 2020, 12, 8592−8603